Control of Mechanical Stratigraphy on Brittle Deformation Style, Northern Snake Range, Nevada

Undergraduate Research Thesis
Submitted in partial fulfillment of the requirements for graduation
with honors research distinction in Earth Sciences
in the undergraduate colleges of
The Ohio State University

By

Caje Antonius Kindred
The Ohio State University
2019

Approved by

W. Ashley Griffith, Advisor
School of Earth Sciences

TABLE OF CONTENTS

ABSTRACT

Bourne (2003) presents a theoretical, layered-elastic model by which fractures can form as a result of mechanical stratigraphy, yet the ability of this model to explain fracture patterns at specific outcrops is still an open question. Hendry's Creek, Nevada is home to outcrops of alternating metasedimentary McCoy Creek Group rocks of the Northern Snake Range Décollement footwall. Layers of mylonitic quartzite and mica schist are distinguished by distinct styles of brittle deformation; quartzite layers exhibit highly concentrated, sub-vertical joints, whereas mica schist layers exhibit conjugate normal fault systems. These layered strata underwent brittle deformation concurrent with exhumation during the mid-Miocene (17 Ma), a process in which the regional stress state would have remained compressive, yet tensile stresses clearly accumulated within quartzite layers. Here, we test the ability of a layered elastic mechanical stratigraphy model, incorporating material properties, thicknesses of sedimentary layers, and tectonic history of rocks to predict the formation and distribution of the two distinct fracture populations observed at Hendry's Creek. High-resolution drone imaging and photogrammetric 3D modelling software enabled extraction of data from an entire cliff face of alternating mica schist and quartzite layers including fracture orientation, concentration, and layer thickness. Structural orientation data provide evidence the two fracture populations are kinematically consistent, however, the order of initiation implied by specific field observations appear to contradict the layered elastic geomechanical model, suggesting a purely elastic model of brittle deformation may fail to accurately demonstrate the role of mechanical stratigraphy.

ACKNOWLEDGEMENTS

First and foremost, I would like to express my appreciation for the generous contributions made by The Edmund M. Spieker Memorial Scholarship, the Friends of Orton Hall fund, The Joseph and Marcia Newhart Scholarship, The Marcus J. and Lottie C. Lieberman Scholarship, and The School of Earth Sciences Field Experience Travel Fund. Without their support, this project would have never come to exist. I would like to thank my research advisor, Dr. W. Ashley Griffith, not only for his time and instruction, but also for supporting me as a geoscientist and continuing to provide me with incredible opportunities. Thank you to Michael Braunagel, especially for your immense help during field work. I would like to recognize both my School of Earth Sciences advisor, Dr. Anne Carey, and my College of Arts & Sciences advisor, Dr. Joanna Spanos, for helping me navigate through my time as an undergraduate at Ohio State. Lastly, I would like to thank my mother for teaching me the importance of hard work and education. She is by far my greatest influence.

List of Figures

List of Tables

INTRODUCTION

Geologic Setting

The field site of Hendry's Creek is located in the Northern Snake Range, a metamorphic core complex located north of Great Basin National Park in eastern Nevada and within the Basin and Range physiographic province. This region today is characterized by crustal extension, and is the culmination of tectonic processes operating since the late Proterozoic including subduction, magmatism, contraction, and extension—both ductile and brittle.

Throughout the Paleozoic and early Triassic Periods, the region of continental crust now known as the Great Basin represented a portion of the prehistoric, western North American passive margin (Stewart and Poole, 1974; Hose and Blake, 1976). During this time, clastic sedimentation resulted in the deposition of sandstones and shales. In the Mesozoic, initiation of eastward subduction of the Farallon Plate resulted in widespread thrust faulting dominating this area, with thin-skin Sevier deformation followed by Laramide thick-skin deformation (Yonkee and Weil, 2015). Continued eastward subduction gave rise to Jurassic-aged mafic intrusions, and coupled with crustal thickening, this process buried rocks, such as the Pre-Cambrian McCoy Creek group, to depths sufficient for regional metamorphism to grades ranging from sub-greenschist to amphibolite facies (Elison, 1995; DeCelles, 2004; Lewis et al., 1999).

Mesozoic crustal shortening was then alleviated by Cenozoic Basin and Range extension. Portions of the underlying Farallon plate falling to the mantle underwent decompression melting from the end of the Paleocene until the Miocene (Van Der Plujim and Marshak, 2004), injecting a large amount of heat below the thickened crust and creating significant gravitational instability. This instability served as a catalyst for Basin and Range extension, coupled with bi-modal magmatism as a passive result to crustal thinning and continued subduction on the western coast of North America (Putirka and Platt, 2012).

This crustal thinning and regional magmatism enabled the formation of metamorphic core complexes throughout the Basin and Range Province, such as that found in the Northern Snake Range, Nevada (Figure 1, site 11). The Northern Snake Range Décollement (NSRD) developed as a ductile-brittle transition zone at 6-7 km depth (Miller et al., 1983). This detachment surface has since been exhumed, revealing the juxtaposition of supracrustal rocks extended by normal faulting onto ductiley deformed igneous and metamorphic rocks (Miller et al., 1983).

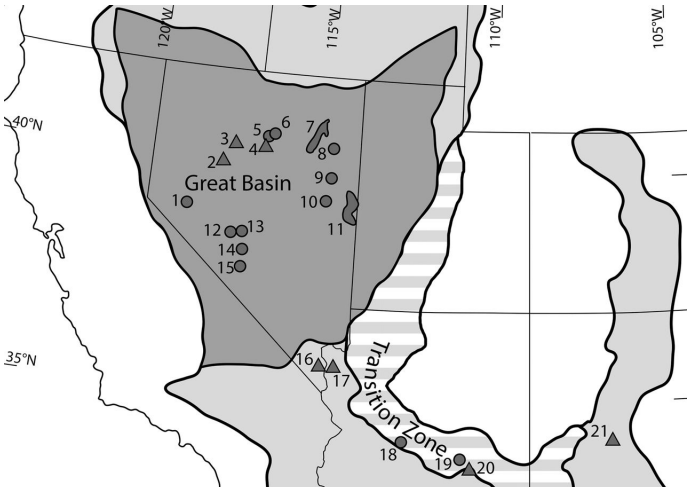

Figure 1. Map depicting the locations of metamorphic core complexes in the Basin and Range Province. Hendry's Creek, the focus of this study, is located within the Northern Snake Range (site 11). Image from Richardson, C. A., and Seedorff, E (2017).

During the Cenozoic, the NSRD experienced asymmetric cooling concurrent with exhumation (Lee et al., 2017). Figure 2 represents the asymmetry of this process, a result of significant rotational strain during elongation. Stretching began in the west, travelling east, and allowing the eastern flank of the Northern Snake Range to remain at depths sufficient for ductile extension up until the early Miocene. This, accompanied by renewed magmatism in the east 24–20 Ma, suggests footwall mylonitization could have continued up until 17 Ma (Miller et al., 1999).

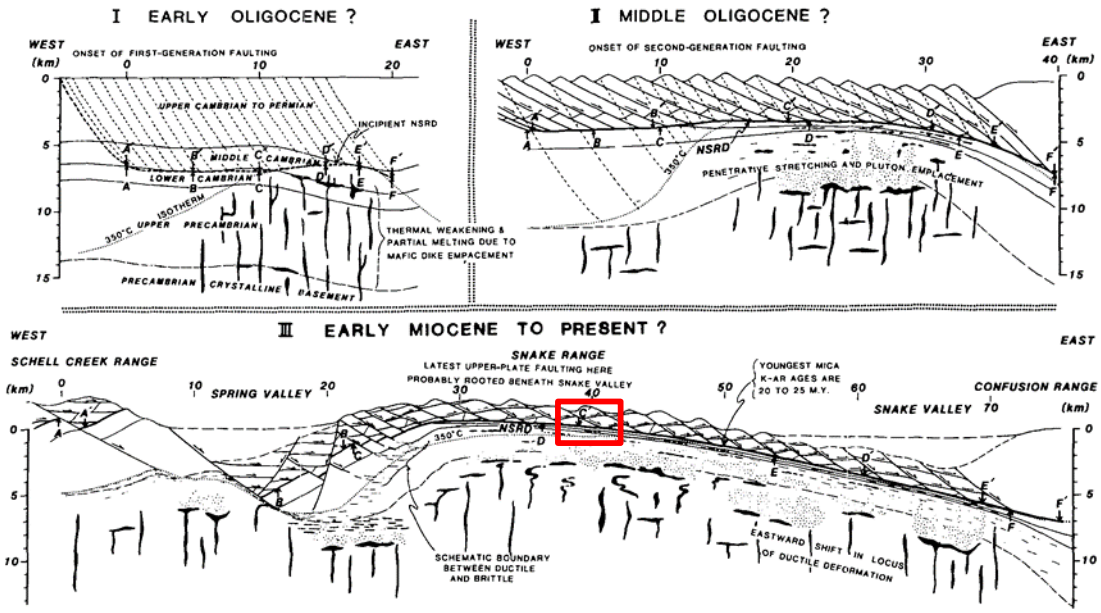

Figure 2. Generalized cross sections portraying the evolution of the Northern Snake Range. The area in red represents the approximate location of Hendry's Creek. Image from Gans et al. (1985).

Hendry's Creek, an incised stream valley on the eastern flank of the Northern Snake Range, displays exhumed layers of McCoy Creek Group mylonitic quartzite and mica schist. These rocks exhibit the characteristic ductile structures associated with the NSRD footwall, however, they also exhibit

overprinting brittle deformation features. Figure 2 implies significant extensional faulting of the upper plate was ongoing in the eastern flank through the early Miocene. This agrees with apatite and zircon fission-track ages, which cluster at 17 Ma indicating rapid cooling during the mid-Miocene (Miller et al., 1999; Lee et al., 2017). The isotherm in Figure 2 also corresponds with temperature estimates around 300–350°C until 17 Ma, when uniform cooling to 100°C took place throughout the range (Miller et al. 1999; Lee et al., 2017). Evidence of this rapid cooling combined with the presence of coarse fanglomerate and rock-avalanche deposits in flanking Tertiary basins (Miller et al., 1983) suggests the observed brittle deformation at Hendry's Creek likely occurred around 17 Ma, during exhumation and just after the youngest boundary of mylonitization.

Mechanical Stratigraphy

Opening-mode fractures, or joints, have been studied throughout the past century, as summarized by Pollard and Aydin (1988). These brittle deformation structures form under conditions when the least principal stress exceeds the tensile strength, yet are commonly found in the subsurface, where the state of stress – including vertical and horizontal principal stresses – is predominantly compressive due to the weight of overburden (McGarr and Gay, 1978; McGarr, 1982). Even when the least principal stress is compressive, joints are still observed at depth (Engelder, 2014). The question remains, how can tensile stress accumulate under remote compression?

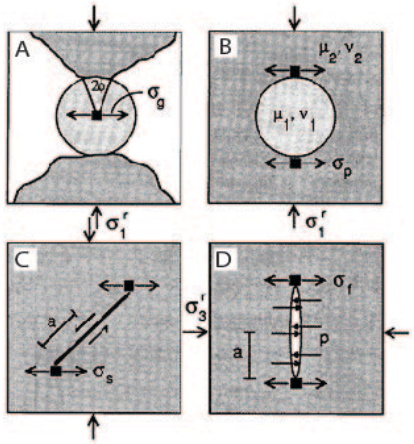

Figure 3. Schematic models of tensile stress accumulation as a result of remote compression. Image from Pollard and Aydin 1988.

Several mechanisms have been shown experimentally and theoretically to induce local tensile stress states. Pollard and Aydin (1988) provided four such idealized explanations for localized tensile stress accumulation as a result of an applied compression (Figure 3). Figure 3A is similar to a Brazilian disc test, where vertical compression results in a horizontal directed tensile stress due to the heterogeneous stress field generated by two applied point loads (Li and Wong, 2013). Figure 3B represents a circular inclusion at depth, in which case a tangential tensile stress accumulates due to the effects of variations in material stiffness. Figure 3C is an inclined flaw at depth accumulating tensile stress as it slides, leading to the development of opening mode wing cracks (Brace and Bombolakis, 1963). Figure 3D represents an internally pressurized elliptical flaw perpendicular to the least compressive stress, allowing tensile stress accumulation along the tips of the flaw. Each of these examples rely on the presence of flaws or inclusions that result in local tensile stress perturbations that lead to joint nucleation.

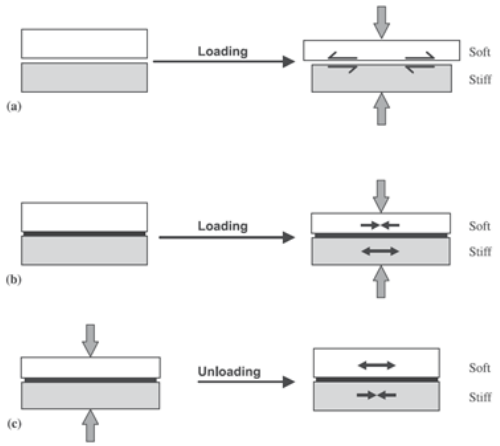

Figure 4. Idealized models of layer-specific behavior as a result of remote compression on a two layered rock system. A) Non-bonded interface subject to vertical compressive loading. B) Bonded interface subject to vertical compressive loading. C) Bonded interface subject to unloading from an initial vertical compressive stress. Figure from Bourne (2003).

Bourne (2003) aims to provide a new mechanism by which tensile stresses can accumulate in layered systems based upon a difference in elastic properties between rock types. First consider a case in which rock layers are not bound to one another (Figure 4a). A normal compressive load applied to two layers would result in a layer-specific amount of extension, relative to the layer's elastic stiffness. The difference in extension would be accommodated by slip between the two stretching layers. Now consider a case in which the system is loaded vertically and the interface between layers is bonded, allowing no inter-layer slip (Figure 4b). The stiffer layer would have a greater resistance to stretching, thus imparting a layer-parallel compressive stress onto the softer layer. On the contrary, the softer layer would be less resistant to stretching, and induce a layer-parallel tensile stress within the stiffer layer. Similarly, a bonded two-layer system being unloaded from a compressive stress state results in layer specific residual stresses (Figure 4c). In this case both layers would contract upon unloading; however, the softer layer would be less resistant to shortening and thus impart a tensile stress within the stiffer layer. The stiffer layer would be more resistant to shortening, and therefore impart a compressive stress within the softer layer. Both cases of a bonded interface (Figures 4b & 4c) provide a mechanism by which tensile stress can accumulate as a result of contrasting elastic properties between two rock layers. This model and the equations given within Bourne (2003), which are summarized below in the Methods section, provide the basis for this study.

Field Site

At Hendry's Creek in the Northern Snake Range, Nevada an exhumed portion of the NSRD footwall displays alternating stratigraphic layers of McCoy Creek Group mylonitic quartzite and mica schist with respectively distinct brittle deformation features. The stiffer quartzite layers have been dominantly fractured by densely populated, vertical joints, whereas the underlying softer mica schist layers have been deformed by conjugate normal fault systems (Figure 5). In relatively thin layers, the opposing style of brittle deformation penetrates beyond the interface of the two rock types. These observations suggest that material properties and layer thickness are likely to have played a role in the brittle deformation observed at Hendry's Creek.

Figure 5. The outcrop at Hendry's Creek, Nevada displaying normal faulted mica-schist (below) and heavily jointed quartzite (above). Person in bottom center for scale.

Footwall deformation in the NSRD was ductile until 17 Ma at the latest, just prior to rapid cooling and exhumation (Miller et al., 1999). Structural orientation measurements of Hendry's Creek made by Miller et al. (1983) provide evidence of kinematic consistency between the ductile fabrics and the brittle deformation as both display a consistent direction of extension (Figure 6). The average orientation of poles to lineations, normal faults, and joint surfaces are equivalent, and represent the direction of maximum elongation. The uniform orientation of these structures suggests that ductile stretching could have occurred up until exhumation had caused enough cooling to enter the brittle realm, upon which brittle deformation and exhumation could occur simultaneously.

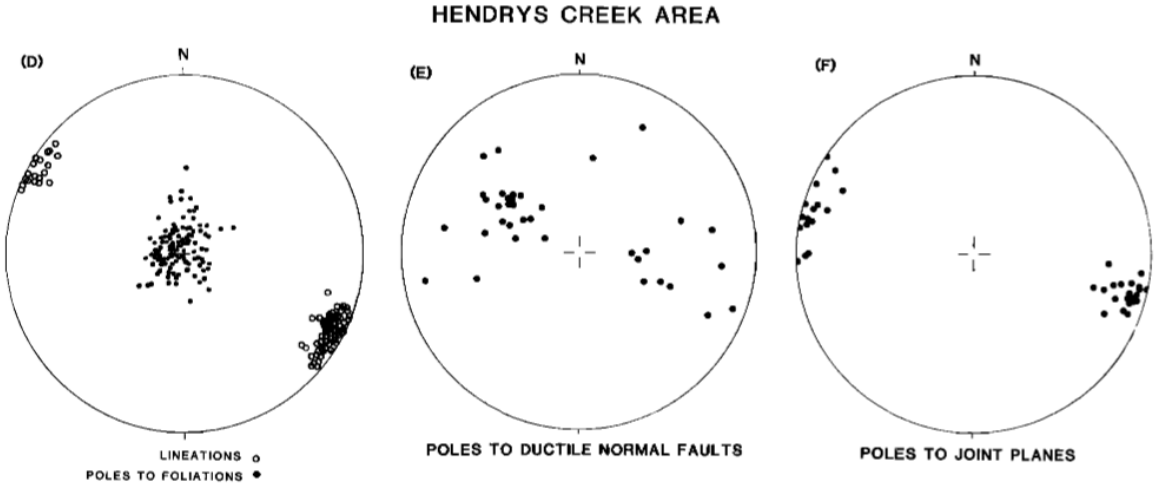

Figure 6. Structural orientation measurements from Hendry's Creek outcrops show kinematic consistency between the ductile and brittle structures. Figure taken from Miller et al. (1983).

The outcrop at Hendry's Creek provides a natural system to test the theoretical model of Bourne (2003). The inter-layered McCoy Creek group's process of transitioning from the ductile to brittle realm during exhumation could be represented as a layered system unloading from an initial remote

compression (Figure 4c). The goal of this study is to represent the brittle deformation process of the Hendry's Creek outcrop by constructing a layered-elastic, geomechanical model which incorporates material properties, individual layer thicknesses, and the tectonic history of the region.

METHODS

Structural Orientation

The initial step toward understanding the relationship between mechanical stratigraphy and brittle deformation style at Hendry's Creek is to measure the thickness of individual mechanical stratigraphic layers and the orientations of the two distinct fracture populations in order to understand their kinematic relationship. This can be accomplished in the field by use of a compass; however, the cliff face at Hendry's Creek is much too tall to make direct measurements across the entire outcrop.

Therefore, the focus of field work was to collect data that enable the construction of a high resolution 3D outcrop model from which attitude and spacing data can be extracted. In order to do so, over 1,000 drone photographs were taken of the Hendry's Creek outcrop. When an image is captured, the DJI Phantom 3 Pro unmanned aerial vehicle (UAV) also records GPS and camera orientation data, which can then be imported with images into Agisoft, a photogrammetric computer program typically used to create 3D models (Figure 7) based on structure from motion algorithms (Blistan et al., 2016; Bemis et al., 2014). Agisoft creates surfaces and depth through geotagged photos and camera orientation data by detecting correspondences between images such as corner points, which possess edges as gradients in multiple directions. The program also uses an algorithm to remove outlier correspondences, assuring features are not matched incorrectly.

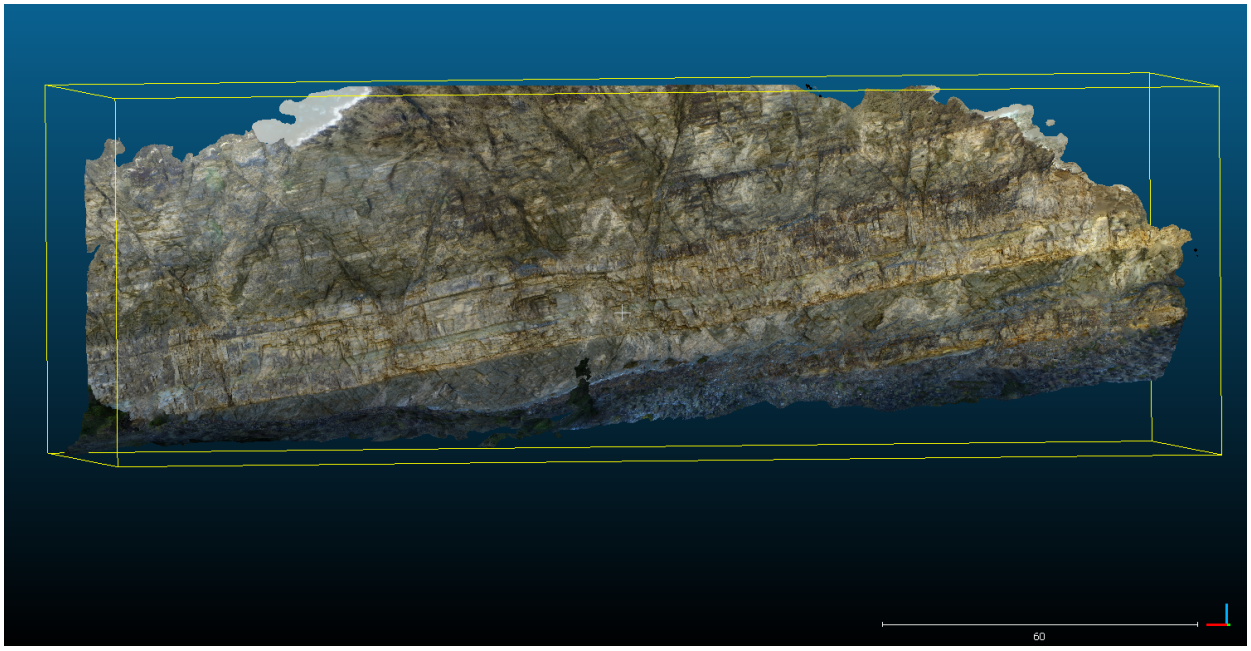

Figure 7. Large scale 3D model of the western side of the McCoy Creek Group outcrop at Hendry's Creek after being imported to CloudCompare. Scale bar in bottom right corner is 60 meters.

The 3D outcrop model was then imported to CloudCompare, a computer program which enables the extraction of distances and structural orientation data (Thiele et al., 2017). Within CloudCompare, manually selected points along fault or joint surfaces can be used to create a plane of best-fit, of which CloudCompare measures the structural orientation. This enables orientation measurements to be taken from the entire cliff face, rather than just the transect along ground level.

Similarly, CloudCompare can measure the distance between two points on the outcrop model. This allows the extraction of individual layer thicknesses and total outcrop height.

Geomechanical Model

In order to determine the influence of mechanical stratigraphy on the brittle deformation at Hendry's Creek, an elastic model composed of *i* layers was constructed to predict the formation of the two distinct fracture populations. Each layer in the model represents a mechanical stratigraphic unit and is assigned a thickness and relevant material properties, including Young's modulus, Poisson's ratio, and cohesive strength. The model considers a three layered system which is exhumed from a remote compressive stress state $(\sigma_{xx}^B, \sigma_{yy}^B, \sigma_{zz}^B)$ while examining the perturbed stress states $(\sigma_{xx}^i, \sigma_{yy}^i, \sigma_{zz}^i)$ created within each individual layer. The layer-dependent stress states arise due to a change in the overburden stress (σ_{yy}) and effects based on coupling with neighboring layers of different elastic properties and thicknesses. In order to calculate the stresses within each layer, the following equations were derived by Bourne (2003) and explained below:

$$\sigma_{xx}^i = \sigma_{xx}^B + M_1\Delta\sigma_{xx+} M_2\Delta\sigma_{zz} - M_4\Delta\sigma_{yy}$$

$$\sigma_{zz}^i = \sigma_{zz}^B + M_1\Delta\sigma_{zz+} M_2\Delta\sigma_{xx} - M_4\Delta\sigma_{yy}$$

$$\sigma_{yy}^i = \sigma_{yy}^B + \Delta\sigma_{yy}$$

The rocks at Hendry's Creek exhibit a single direction of elongation. Therefore, in order to assure uniaxial extension occurs, the shear stress components $(\sigma_{xy}^i, \sigma_{yz}^i, \sigma_{zx}^i)$ are set to equal zero, and thus the layered system experiences no rotation.

$$\sigma_{xy}^i = \sigma_{yz}^i = \sigma_{zx}^i = 0$$

The coupling coefficients (M_1, M_2, M_4) are calculated based on the thickness averaged coupling moduli (m_1, m_2, m_4) and the individual layers' coupling moduli $(m_{1,i}, m_{2,i}, m_{4,i})$. The overbars indicate thickness averaged values:

$$m_{1,i} = \frac{E_i}{1 - v_i^2}$$

$$m_{2,i} = \frac{E_i v_i}{1 - v_i^2}$$

$$m_{4,i} = \frac{v_i}{1 - v_i}$$

$$m_1 = \overline{m_{1,i}}, m_2 = \overline{m_{2,i}}, m_4 = \overline{m_{4,i}}$$

where E is the Young's modulus and v is Poisson's ratio. The coupling coefficients are then solved by:

$$M_1 = \frac{m_1 m_{1,i} - m_2 m_{2,i}}{m_1^2 - m_2^2}$$

$$M_2 = \frac{m_1 m_{2,i} - m_2 m_{1,i}}{m_1^2 - m_2^2}$$

$$M_4 = m_4 \frac{m_{1,i} + m_{2,i}}{m_1 + m_2} - m_{4,i}$$

The first coupling modulus, M_1, is defined always to be positive and, for negligible differences in Poisson's ratio, representative of the ratio of a layer's Young's modulus to the thickness-averaged Young's modulus. The second coupling modulus, M_2, is defined to be positive for layers with greater than average Poisson's ratio and, for negligible differences in Poisson's ratio, is equal to zero. The fourth coupling modulus, M_4, assuming negligible differences in Poisson's ratio, is positive for stiffer than average layers and negative for softer than average layers (Bourne, 2003).

The coupling coefficients maintain static equilibrium between the sum of thickness averaged stresses in each layer and the regional stress and can be interpreted as a measure of an individual layer's contribution to the system's elastic behavior (Figure 8). A vertical compression results in layer-parallel elongation, and the thickness averaged stresses, σ_{xx}^i, are related to the stress on a rigid platen, σ_{xx}^P:

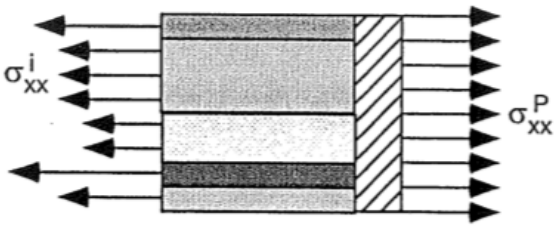

$$\sigma_{xx}^P T = \sum \sigma_{xx}^i t^i$$

Figure 8. 2D representation of individual layers, *i*, and their respective horizontal stresses, σ_{xx}^i. Their respective stress states are calculated based on the total horizontal stress, σ_{xx}^P, total thickness, *T,* and the relative layer's thickness, t^i.

The geomechanical model configures the stress path of each individual layer by calculating the stress perturbation due to a change in overburden during exhumation from a given initial depth to a given final depth. The depth of fracture initiation in each layer can then be estimated by adopting the Griffith (1924) criterion for microscopic tensile failure, a function of bulk cohesive strength:

$$\sigma_{xx}^i \geq \frac{1}{2} C_i$$

and the modified Coulomb criterion for macroscopic shear failure (Jaeger et al., 2009), a function of bulk cohesive strength and internal friction:

$$\frac{1}{2}(\sigma_1 - \sigma_3) \geq C_i \cos(\phi_i) - \frac{1}{2}(\sigma_1 + \sigma_3) \sin(\phi_i)$$

Since the rocks at Hendry's Creek were exhumed within a normal faulting environment (i.e., Basin and Range extension), it is necessary to provide an appropriate initial state of stress for the model. Therefore, we developed a function within MATLAB which calculates the state of stress optimally oriented for slip along a given fault angle, θ, internal coefficient of friction, μ and pore-fluid factor, λ (Sibson, 1974):

$$\sigma_{yy}^B = \rho g d(1 - \lambda)$$

$$\sigma_{xx}^B = \sigma_{yy}^B - \frac{R}{1 + R}$$

$$\sigma_{zz}^{B} = \frac{\sigma_{xx}^{B} + \sigma_{yy}^{B}}{2}$$

where:

$$R = \frac{\sin(2\theta) + \mu\,(\cos(2\theta) + 1)}{\sin(2\theta) + \mu\,(co\,s(2\theta) - 1)}$$

This calculation for initial stress based on shear failure of an optimally oriented fault assumes that the greatest compressive, horizontal principal stress is equal to the average of the vertical principle stress and the least compressive, horizontal principal stress (Sibson, 1974).

Table 1. Relevant parameterized values of bulk and material properties used to construct the geomechanical model.

Bulk Model Properties		Layer Specific Material Properties		
Coefficient of Thermal Expansion	10^{-5} °C^{-1} [T]		Quartzite	Mica Schist
Density	2650 kg/m^3 [S]	Young's Modulus	80 GPa [DU]	30 GPa [DU, Z]
Pore Fluid Factor	0.4 [S]	Poisson's Ratio	0.23 [Q]	0.2 [Z]
Coefficient of Friction	0.75 [S]	Cohesive Strength	15 GPa [S, Q]	1.5 GPa [Z]

[S] (Tievuan, 2016), [MS] (Zhang, et al., 2011), [DU] (Durham University), [T] (Robertson, 1988), [Q] (Abdullah and Singh, 2010)

RESULTS

Construction of 3D Model

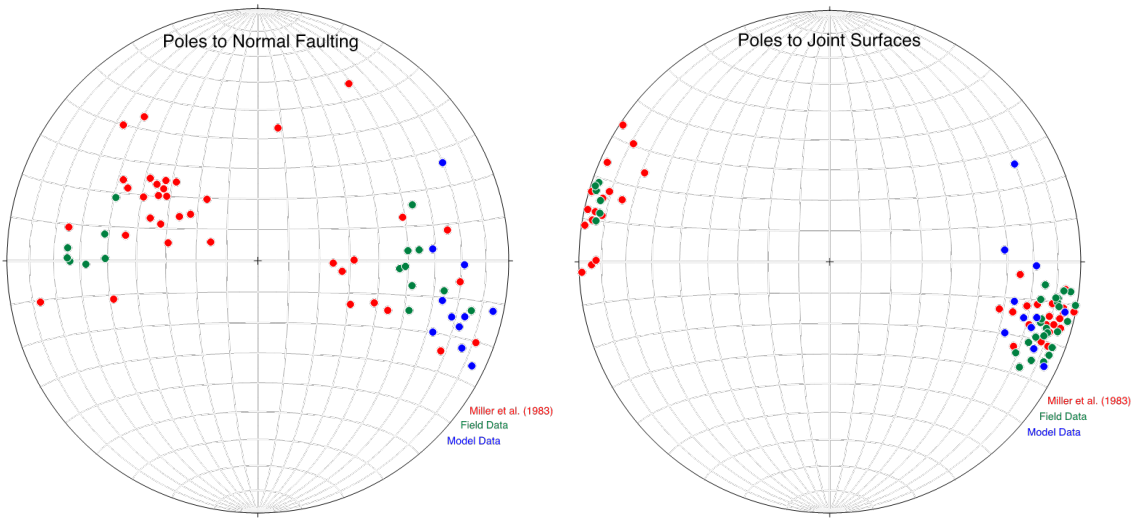

Figure 9. Comparison of structural orientation data extracted from the 3D outcrop model to measurements made in the field and to those reported in Miller et al. (1983).

In order to validate the 3D outcrop model and the data extracted using CloudCompare, the resulting orientation measurements are plotted in Figure 8 with measurements of the same features made in the field and by Miller et al. (1983). The 3D outcrop model provides joint orientations that are remarkably consistent both with the current field measurements and those measurements reported by Miller et al. (1983). Although orientation data of the normal faults have much greater scatter, this is consistent with observations made in the field. The direction of greatest stretching for the quartzite joints is equivalent to the orientation of their poles, or in other words, normal to the joint surface. In normal faults, stretching takes place roughly 30 degrees from the pole of the normal fault. Therefore, the average orientation of maximum elongation of these two deformation styles is approximately equivalent, suggesting normal faulting and jointing are kinematically consistent as explained by Miller et al. (1983). Reproduction of those results validates not only the outcrop model but also the extracted data.

There are seven distinctly mappable units from Hendry's Creek within the 3D outcrop model. The thickness of these units can be measured within CloudCompare by manually selecting points along the respective upper and lower contacts. The units and their thicknesses are compiled below, listed from top to bottom of the outcrop. The geomechanical model tests three-layered packages, and thus five different scenarios are possible—three quartzite-centered and two schist-centered.

Table 2. Thickness of stratigraphic layers of the McCoy Creek Group at Hendry's Creek from top (left) to bottom (right) and the different scenario numbers.

Rock Type	Schist	Quartzite	Schist	Quartzite	Schist	Quartzite	Schist
Thickness (m)	17	1.5	10.5	2.5	0.5	7.5	11
Quartzite -Centered Scenarios	1		2		3		
Schist-Centered Scenarios		4				5	

Specific Field Observations

Some specific field observations help to illustrate the style of fracturing in the McCoy Creek Group at Hendry's Creek, as well as the role of mechanical stratigraphy in controlling fracture behavior. I summarize three specific observations below such as sigmoidal normal faults in a thin schist layer, a conjugate normal fault system, and heterogeneous joint concentration near a layer interface (Figures 10, 11, 12). Specifically, these observations shed light on the role of relative thickness of individual layers, the development of conjugate normal faults in thick schist layers, and the interaction between normal faulting in schist layers and joint initiation in quartzite layers.

The mica schist layers at Hendry's Creek are dominated by normal faulting. Within thick mica schist layers the attitude of normal faulting is relatively consistent, however, in thin mica schist layers bound by thicker quartzite layers the attitude of normal faulting varies in an almost sigmoidal fashion (Figure 9). At the upper and lower contacts of this thin mica schist layer, fault dip is sub-parallel to jointing.

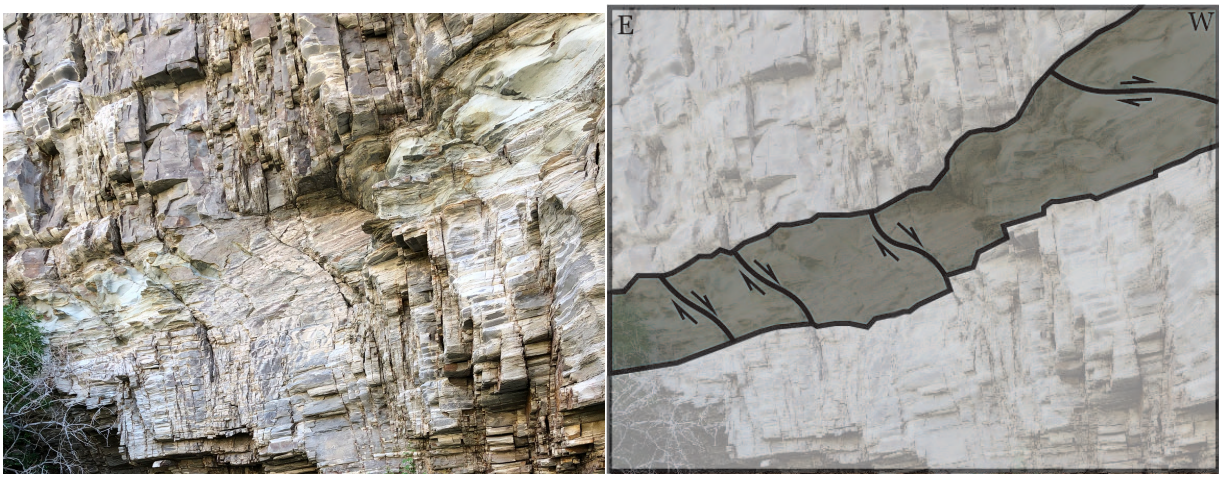

Figure 10. Sigmoidal variation in fault attitude within a thin mica schist layer bound by thicker quartzite layers.

A conjugate fault system within a relatively thick schist layer displays a single east-dipping fault, where several smaller scale west-dipping faults truncate (Figure 10). It seems likely that the east-dipping fault represents the dominant orientation, with each episode of its slip preserved by the

smaller-scale western dipping normal faults. These smaller scale faults also appear to have propagated fractures into the footwall of the dominant fault.

Figure 11. Conjugate fault system displayed within a layer of mica schist at Hendry's Creek. The eastern dipping fault (marked by the red fault symbol) appears to be the dominant orientation, with smaller-scale western dipping faults preserving episodes of slip along the dominant fault. A backpack is shown in the photo for scale.

The quartzite layers at Hendry's Creek are dominated by sub-vertical jointing. In many areas, the spacing between joints is much smaller than layer thickness. There is, however, heterogeneity in the concentration of joints throughout the outcrop. Some of the densest areas appear to be along the interface between opposing rock types, specifically where large normal faults of mica schist layers terminate into a quartzite layer. The concentration also decreases with increasing distance from the interface between layers.

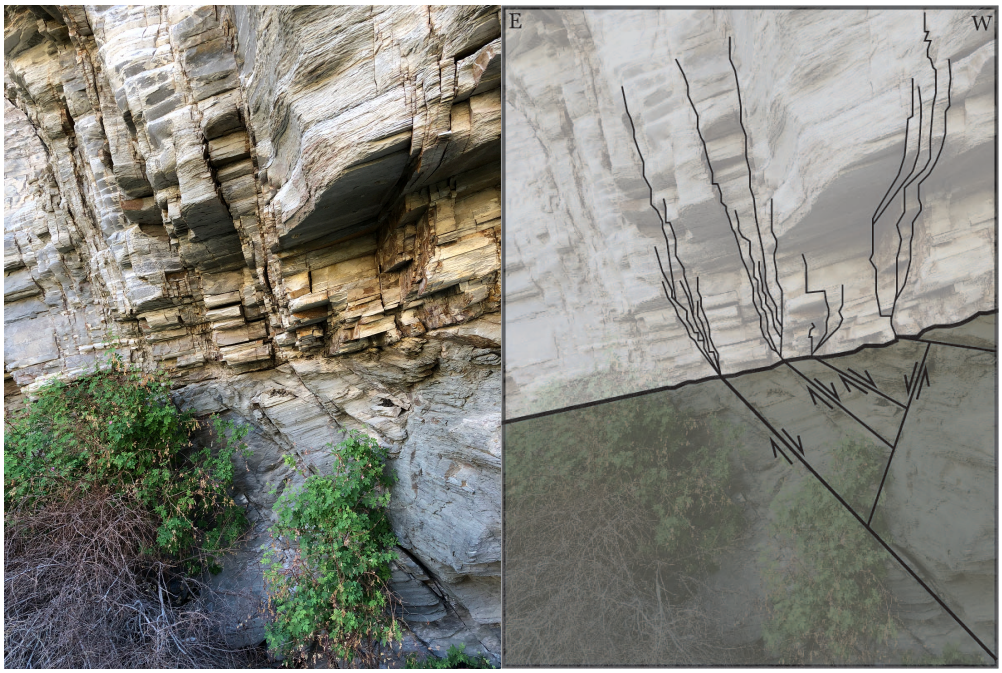

Figure 12. Joint concentration is greatest near the termination of mica schist normal faults, and concentration decreases as distance from the interface increases.

Geomechanical Model

The differential stress between σ_{yy}^{i} and σ_{xx}^{i}, along with the overburden, σ_{yy}^{i}, approach zero as the exhumation process reaches the surface (Figure 13). This is due to the assumption that the surface of the Earth is a free surface, and thus it cannot support any stress. Similarly, σ_{xx}^{i} and σ_{zz}^{i} begin the exhumation process as compressive, with σ_{zz}^{i} being the greater horizontal compressive stress. These values become increasingly tensile through the exhumation process, and by the role of mechanical stratigraphy (e.g., the coupling moduli, which account for differences in material properties) the horizontal principle stresses trade orientation. By the end of the modeled exhumation, σ_{zz}^{i} becomes the least horizontal compressive stress, reaching a tensile value within the quartzite layer at roughly 1000 meters depth.

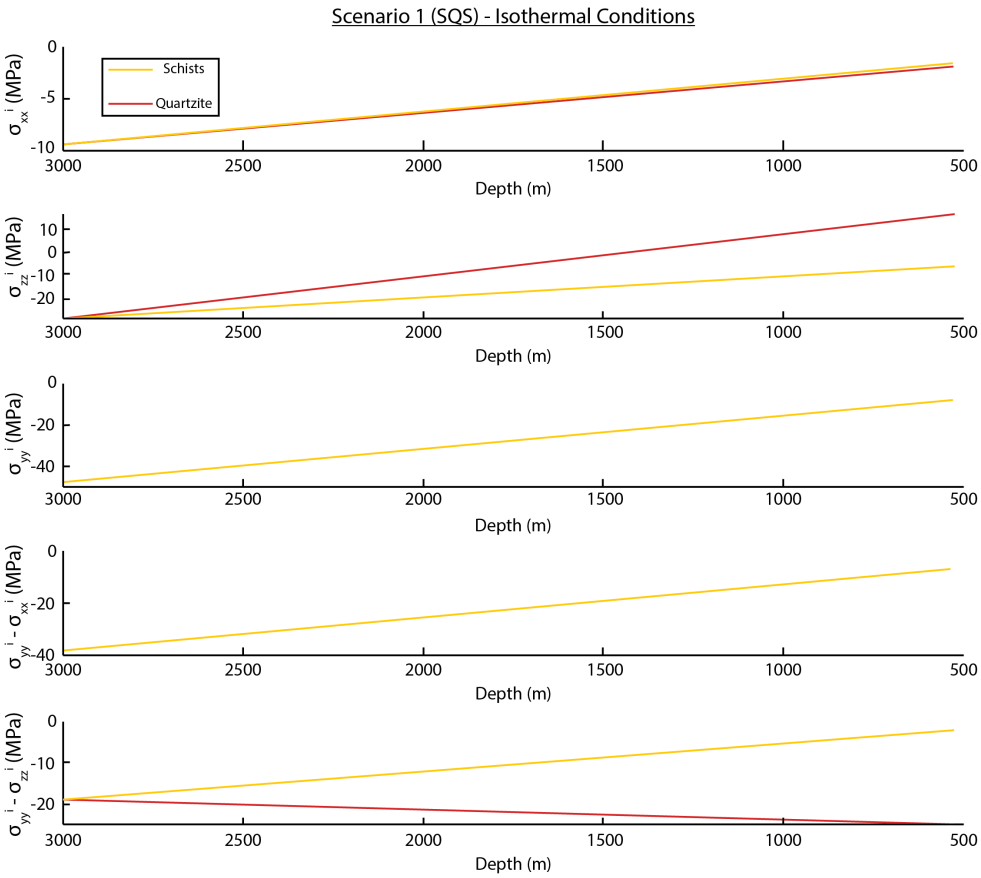

Figure 13. Stress paths of each layer during exhumation under isothermal conditions.

This rotation of the principal stresses proves to be significant, because σ_{zz}^{i} within the quartzite layer reaches a sufficiently high value to initiate tensile failure within scenarios 1 and 2. Shear failure, however, is not initiated within any layer under isothermal conditions, meaning the lack of a thermal stress component may serve as a downfall for the elastic model.

The rocks at Hendry's Creek are understood to have cooled concurrently with exhumation (Miller et al., 1999). Based on the assumption of an isotropic thermal expansion, the equations for the individual layer stresses become:

$$\sigma_{xx}^{i} = \sigma_{xx}^{B} + M_1\Delta\sigma_{xx+}\, M_2\Delta\sigma_{zz} - M_4\Delta\sigma_{yy} - \frac{\alpha E_i \Delta T}{1-v}$$

$$\sigma_{zz}^{i} = \sigma_{zz}^{B} + M_1\Delta\sigma_{zz+}\, M_2\Delta\sigma_{xx} - M_4\Delta\sigma_{yy} - \frac{\alpha E_i \Delta T}{1-v}$$

$$\sigma_{yy}^{i} = \sigma_{yy}^{B} + \Delta\sigma_{yy} - \frac{\alpha E_i \Delta T}{1-v}$$

where α is the coefficient of thermal expansion. This additional term represents the stress associated with thermal expansion, and its inclusion leads to potentially more accurate results.

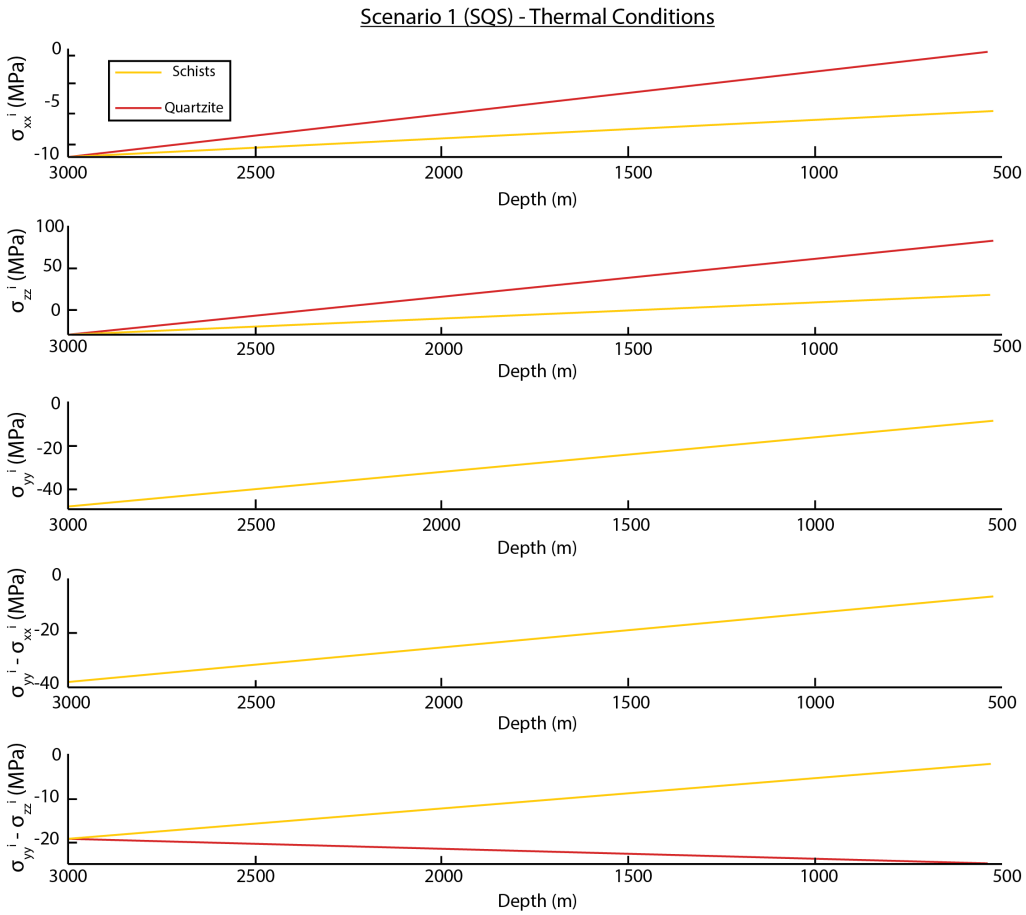

Figure 14. Stress paths of each layer during exhumation under thermal conditions.

Just as before the horizontal principle stresses $(\sigma_{xx}^{i},\ \sigma_{zz}^{i})$ become increasingly tensile through exhumation, and the differential stresses approach zero $(\sigma_{yy}^{i} - \sigma_{xx}^{i},\ \sigma_{yy}^{i} - \sigma_{zz}^{i})$ (Figure 14). The difference, however, lies in the initiation of deformation. Under thermal conditions, tensile failure of the quartzite layers precedes shear failure of the mica schist layers, both in the direction of σ_{zz}^{i}, in scenarios 1, 2, and 4. The rotation of the principal stresses is still present but the thermal component of stress is significant enough to permit the formation of both distinct fracture types. Scenarios 3 and 5, under thermal conditions, result in tensile failure of quartzite layers proceeded by further tensile failure within mica schist layers. There is an apparent uncertainty around this thermal stress. Scenarios 3 and 5 under thermal conditions both fail to represent accurately the two fracture populations found at Hendry's Creek. However, scenarios 1, 2, and 4 succeed.

DISCUSSION

The field observations (Figures 10, 11, 12) provide clues to the influences of mechanical stratigraphy and the brittle deformation shown at Hendry's Creek. The relatively thin mica schist layer bound by quartzite layers is an example of how layer thickness can influence the orientation of deformation (Figure 10). At the layer interfaces, the sigmoidal faults share a sub-vertical dip with quartzite joints. It appears as though the fracture propagated from one quartzite layer into the relatively thin schist and began to refract into the form of a normal fault. As the fracture progressed completely through the schist layer it refracted again, returning to the sub-vertical dipping orientation of quartzite joints.

It appears that quartzite joints have propagated from mica schist normal fault tips along the interface between the two rock types, where joint concentration is relatively high (Figure 11). This implies that normal faulting within mica schist occurred first and most likely aided in the opening of quartzite joints. The decline in concentration of joints with distance from the interface (Figure 11) simply may be a result of stress shadowing; as joints propagate, the infinitesimally small surface area of the tip is a free surface (Gross et al., 1995). Therefore, as joints propagate in close proximity to each other, it is possible for one joint to alleviate the driving stress field of a neighboring joint. The joints reaching the furthest distances from the interface are those that have cast stress shadows upon their neighbors.

In the isothermal scenarios of the geomechanical model, shear failure failed to initiate at all. Tensile failure, however, occurred in direction of σ_{zz}^{i} as a result of rotation of principal stresses within individual layers. Due to the coupling coefficients and their influence on the stress paths, the least and greatest horizontal principal stresses actually trade orientations. Although the system was initially prepped for extensional failure in the direction of σ_{xx}^{i}, tensile failure is calculated to occur in the direction of σ_{zz}^{i}.

Incorporation of the thermal component of stress to scenarios 1, 2, and 4 leads to tensile failure of quartzite followed by shear failure of mica schist. These styles of deformation correspond with those observed at Hendry's Creek but field observations suggest the order of fracturing was reversed. If tensile failure were to have preceded shear failure, perhaps normal faulting of mica schist layers acted to enhance the fracturing of quartzite layers and therefore increased the joint concentration.

There are many possibilities for explaining the discrepancy between the field observations and the geomechanical model. The results of the geomechanical model seem to underestimate the role of each layer's thickness, because the results are only dependent on the relative thickness contributions of the two types of material properties (i.e., quartzite and mica schist). The parameterized values for material properties (i.e., Young's modulus, Poisson's ratio, cohesion, thermal expansion coefficient) may not be accurate for the rocks found at Hendry's Creek and could be better understood by laboratory experimentation. Regional conditions (i.e., thermal gradient, pore fluid factor) may also differ from the assumed values.

The stress associated with thermal expansion was assumed to be isotropic, which may be incorrect in describing the thermal history of Hendry's Creek. A misrepresented thermal gradient could then propagate the error even further. It is also possible that an elastic model is not entirely representative of the process which lead to the deformation observed at Hendry's Creek. Perhaps there is a plastic component to the deformation, which appears to be quite possible with the relative timing of exhumation and youngest mylonitization. The geothermal gradient of the Northern Snake Range in the mid-Miocene was much higher than the average 25°C per kilometer (Figure 2; Miller et al. 1999).

The geomechanical model provides valuable insight into the formation of layer-specific stress states in the cases of bonded interfaces but the model should be approached with caution when applied to tangible contemporaries such as the McCoy Creek Group outcrop in this study.

CONCLUSIONS

This study sought to adapt the model of Bourne (2003) into a geomechanical model of the process which lead to brittle deformation of the McCoy Creek Group rocks at Hendry's Creek. The brittle deformation of the outcrop at Hendry's Creek appears to have been influenced by mechanical stratigraphy (e.g., Figures 10, 11, 12). Bourne (2003) provided a theoretical model in which a regional stress on a layer-bonded sequence can result in interlayer stresses dependent upon material properties. Field observations suggest mechanical stratigraphy played a role in brittle deformation:

- Brittle deformation manifested primarily dependent upon the material properties of individual layers. Quartzite layers, which are much stiffer, have been fractured by sub-vertical opening mode fractures. In contrast, the much softer mica schist layers have been fractured by conjugate normal fault systems with an east-dipping dominant orientation.
- Relative layer thickness seems to influence the style of deformation, where a thin schist layer bound by thick quartzite layers possesses sigmoidal normal faults, which are sub-parallel to joint orientation at their upper and lower contacts (Figure 10).
- Large scale normal faults of mica schist layers which truncate into a quartzite contact appear to have aided in the formation of joints within quartzite layers. Joint concentration dissipates with increasing distance from the interface (Figure 12).

The geomechanical model produces jointing of quartzite layers followed by normal faulting of mica schist layers in three of ten cases, all of which required the stress associated with thermal expansion to produce shear failure of mica schist layers. In these three cases, a rotation of horizontal principal stresses takes place allowing deformation to form in a direction normal to that of which the system was primed for failure. Although mica schist normal faults seem to have assisted in the initiation of quartzite tensile failure, this does not mean tensile failure occurred exclusively via normal faults. It may be true that the geomechanical model accurately predicts the order in which deformation styles initiated, and the onset of normal faulting assisted in second generation jointing of quartzite layers.

Recommendations for Future Work

The geomechanical model produced in this study could be adapted to tectonic histories of any layered stratigraphic sequence, and could therefore be applied to many other field sites. Improvements could also be made on the specific model constructed for Hendry's Creek such as:

- Experimenting from different initial stress states
- Representing the stresses associated with thermal expansion in a non-isotropic manner
- Developing a model which considers individual layer thickness, rather than relative material properties' contribution to the total thickness
- Incorporating a ductile component of deformation

The 3D outcrop model provides many possibilities for future work, with access to extractable data from the entire Hendry's Creek outcrop such as fracture orientation, spacing, and layer thickness. Heterogeneity in joint concentration may offer further insight into the order in which each fracture type initiated, based on the number of jointing generations present.

REFERENCES CITED

Abdullah, Hasan, and Sukhdev Singh. Laboratory Evaluation of Five Quartzites. Proc. *Indian Geotechnical Conference-2010*, Mumbai. (2010).

Bemis, Sean P., Steven Micklethwaite, Darren Turner, Mike R. James, Sinan Akciz, Sam T. Thiele, and Hasnain Ali Bangash. Ground-based and UAV-based photogrammetry: A multi-scale, high-resolution mapping tool for structural geology and paleoseismology. *Journal of Structural Geology* 69 (2014): 163-178.

Blistan, Peter, Ľudovít Kovanič, Vladislava Zelizňaková and Jana Palková. Using UAV photogrammetry to document rock outcrops. *Acta Montanistica Slovaca* 21.2 (2016).

Bourne, S. J. Contrast of elastic properties between rock layers as a mechanism for the initiation and orientation of tensile failure under uniform remote compression. *Journal of Geophysical Research, 108*(B8) (2003).

Brace, W. F., and Bombolakis, E. G. A note on brittle crack growth in compression. *Journal of Geophysical Research 68*(12) (1963): 3709-3713.

DeCelles, Peter G. Late Jurassic to Eocene evolution of the Cordilleran thrust belt and foreland basin system, western USA. *American Journal of Science* 304.2 (2004): 105-168.

Elison, Mark W. Causes and consequences of Jurassic magmatism in the northern Great Basin: Implications for tectonic development. *Special Papers – Geological Society of America* (1995): 249-249.

Engelder, Terry. Stress regimes in the lithosphere. Vol. 151. Princeton University Press (2014).

Gans, P. B., E.L. Miller, J. McCarthy, and M.L. Ouldcott. Tertiary extensional faulting and evolving ductile-brittle transition zones in the northern Snake Range and vicinity: New insights from seismic data. *Geology* 13.3 (1985): 189-193.

Griffith, A. A. Proceedings of the First International Congress on Applied Mechanics. (1924): 55-63.

Gross, Michael R., Mark P. Fischer, Terry Engelder, and Roy J. Greenfield. Factors controlling joint spacing in interbedded sedimentary rocks: integrating numerical models with field observations from the Monterey Formation, USA. *Geological Society, London, Special Publications* 92.1 (1995): 215-233.

Hose, Richard K., and M. Clark Blake Jr. Geology and mineral resources of White Pine County, Nevada. No. 85. University of Nevada (1976).

Jaeger, John Conrad, Neville GW Cook, and Robert Zimmerman. Fundamentals of rock mechanics. Hoboken, New Jersey: John Wiley & Sons (2009) 90-94.

Lee, Jeffrey, Terrence Blackburn, and Scott Johnston. Timing of mid-crustal ductile extension in the northern Snake Range metamorphic core complex, Nevada: Evidence from U/Pb zircon ages. *Geosphere* 13.2 (2017): 439-459.

Lewis, Claudia J., Brian P. Wernicke, Jane Selverstone, and John M. Bartley. Deep burial of the footwall of the northern Snake Range decollement, Nevada. *Geological Society of America Bulletin* 111.1 (1999): 39-51.

Li, D., and Wong, L. N. Y. The Brazilian disc test for rock mechanics applications: review and new insights. *Rock mechanics and rock engineering*, 46(2) (2013): 269-287.

McGarr, A. Analysis of states of stress between provinces of constant stress. *Journal of Geophysical Research: Solid Earth* 87.B11 (1982): 9279-9288.

McGarr, Arthur, and N. C. Gay. State of stress in the Earth's crust. *Annual Review of Earth and Planetary Sciences* 6.1 (1978): 405-436.

Miller, E. L., Gans, P. B., and Garing, J. The Snake Range Décollement: An exhumed Mid-Tertiary ductile-brittle transition. *Tectonics, 2*(3) (1983): 239-263.

Miller, Elizabeth L., Trevor A. Dumitru, Roderick W. Brown, and Phillip B. Gans. Rapid Miocene slip on the Snake Range–Deep Creek range fault system, east-central Nevada. *Geological Society of America Bulletin* 111.6 (1999): 886-905.

"Modulus of Elasticity." Foundations - Modulus of Elasticity, Durham University, http://community.dur.ac.uk/~des0www4/cal/dams/geol/mod.htm.

Pollard, David D., and Atilla Aydin. Progress in understanding jointing over the past century. *Geological Society of America Bulletin* 100.8 (1988): 1181-1204.

Putirka, Keith, and Bryant Platt. Basin and Range volcanism as a passive response to extensional tectonics. *Geosphere* 8.6 (2012): 1274-1285.

Richardson, C. A., and Seedorff, E. Estimating friction in normal fault systems of the Basin and Range province and examining its geological context. *Geological Society, London, Special Publications, 458,* 1 (2017): 155-179

Robertson, Eugene C. "Thermal properties of rocks." Open-File Report No. 88-441. US Geological Survey, 1988.

Sibson, Richard H. Frictional constraints on thrust, wrench and normal faults. *Nature* 249.5457 (1974): 542.

Stewart, J. H., and F. G. Poole. Lower Paleozoic and uppermost Precambrian Cordilleran miogeocline, Great Basin, western United States. *The Society of Economic Paleonotologists and Mineralogists: Tectonics and Sedimentation,* SP22 (1974): 28-57.

Thiele, S. T., Grose, L., Samsu, A., Micklethwaite, S., Vollgger, S. A., and Cruden, A. R. Rapid, semi-automatic fracture and contact mapping for point clouds, images and geophysical data. *Solid Earth*, *8*(6) (2017): 1241.

Miller, E.L., The North American Cordillera, in Van der Pluijm, Ben A., and Stephen Marshak. Earth Structure. New York, NY: W. W. Norton & Company (2004) 198-207.

Yonkee, W. Adolph, and Arlo Brandon Weil. Tectonic evolution of the Sevier and Laramide belts within the North American Cordillera orogenic system. *Earth-Science Reviews* 150 (2015): 531-593.

Zhang, Xiao-Ping, Louis Ngai Yuen Wong, Si-Jing Wang, and Geng-You Han. Engineering properties of quartz mica schist. *Engineering geology* 121.3-4 (2011): 135-149.

Zhu, Tieyuan. Some Useful Numbers on the Engineering Properties of Materials (Geologic and Otherwise). 2016. PDF file.

APPENDICES

Appendix A: Script for Isothermal Exhumation

```
clear all
clc

%Define thicknesses of individual layers (17, 1.5, 10.5, 2.5, 0.5, 7.5, 11)
a = 17;
b = 1.5;
c = 10.5;
t = [a b c]; %thickness (meters)

%Define specific scenario parameters

    %SQS
    E = [30 80 30]*10^9;            %Young's moduli (Pa)
    nu = [0.2 0.23 0.2];            %Poisson's ratio
    C = [1.5 15 1.5]*10^6;          %cohesive strength of each layer (Pa)
(SomeUsefulNumbers & Zhang, 2011 Table 6)

% %     %QSQ
%     E = [80 30 80]*10^9;            %Young's moduli (Pa)
%     nu = [0.23 0.2 0.23];           %Poisson's ratio
%     C = [15 1.5 15]*10^6;           %cohesive strength of each layer (Pa)
(SomeUsefulNumbers & Zhang, 2011 Table 6)

%Define non-specific scenario parameters
alpha = 10*10^-6;                   %thermal expansion coefficient (1/C)
rho = 2650;                         %density (kg/m^3)
g = 10;                             %grav acceleration (m/s^2)
N = length(E);                      %number of layers
M = 100;                            %number of iterations
lm = 0.4;                           %pore fluid factor (ratio of hydrostatic to
lithostatic pressure gradient)
mu = 0.75;                          %coeff of friction (SomeUsefulNumbers 0.5-0.8)
theta = 30*pi/180;                  %angle of internal friction

%Define individual layer coupling moduli (5 in Bourne, 2003)
m1i = E./(1- (nu).^2);
m2i = (nu.*E)./(1-(nu).^2);
m4i = nu./(1-nu);

%Define thickness averaged coupling moduli (6 in Bourne, 2003)
m1 = sum(m1i.*t)./sum(t);
m2 = sum(m2i.*t)./sum(t);
m4 = sum(m4i.*t)./sum(t);


%Define compound coupling moduli (8 in Bourne, 2003)
M1 = ((m1*m1i) - (m2*m2i))./(m1.^2-m2.^2);
M2 = ((m1*m2i) - (m2*m1i))./(m1.^2-m2.^2);
M4 = m4*((m1i+m2i)./(m1+m2))-m4i;
```

```
%Define regional stress path
h0 = 3000;              %initial depth
hf = 500;               %final depth
Tgrad = 25;             %geothermal gradient (degrees C per km)
T0 = Tgrad*h0./1000;    %starting temperature
Tf = Tgrad*hf./1000;    %final temperature

%Sibson Normal Fault Tensor
[syyb, sxxb, szzb] = Sibson_NormalFaultTensor(h0,lm,mu);        %calculate initial
stress state assuming normal faulting environment
sxxb = -sxxb*10^6;syyb = -syyb*10^6; szzb = -szzb*10^6;            %initial stress
state (Pa)

[syyf, sxxf, szzf] = Sibson_NormalFaultTensor(hf,lm,mu);        %calculate final
stress state assuming normal faulting environment
sxxf = -sxxf*10^6;syyf = -syyf*10^6; szzf = -szzf*10^6;            %final stress state
(Pa)

%Stress and Temperature Changes for Each Iteration
dsyy = linspace(0,(syyf-syyb), M+1);                            %vertical (greatest
compressive) stress path
dsxx = linspace(0,(sxxf-sxxb), M+1);                            %least compressive
stress path
dszz = linspace(0,(szzf-szzb), M+1);                            %intermediate
compressive stress path
dT = linspace(0,Tf-T0, M+1);                                    %temperature change

%Intialize layer stresses
sxxi = zeros(M,N);
syyi = zeros(M,N);
szzi = zeros(M,N);
syyi_isothermal = zeros(M,N);

for m = 1:M                                                     %loop that iterates
through each stress change increment
    for i = 1:N                                                 %loop that iterates
through each layer
        sxxi(m,i) =  sxxb + M1(i)*dsxx(m) + M2(i)*dszz(m) - M4(i)*dsyy(m); %(7 in
Bourne, 2003)
        szzi(m,i) =  szzb + M1(i)*dszz(m) + M2(i)*dsxx(m) - M4(i)*dsyy(m);
        syyi(m,i) =  syyb + dsyy(m);
    end
end

depth = syyi./(rho*g*(1-lm));                          %depth (meters)

%Plot stress paths in each individual layer
figure,
subplot 511, plot(depth, sxxi.*10.^-6) %plot(sxxi(:,1)), hold on, plot(sxxi(:,2))
legend('Schist', 'Quartzite', 'Schist'),
ylabel('\sigma_{xx}^i (MPa)'), xlabel('Depth (m)')

subplot 512, plot(depth,szzi.*10.^-6) %plot(sxxi(:,1)), hold on, plot(sxxi(:,2))
```

```
%legend('Schist', 'Quartzite', 'Schist'),
ylabel('\sigma_{zz}^i (MPa)'), xlabel('Depth (m)')

subplot 513, plot(depth,syyi.*10.^-6) %plot(sxxi(:,1)), hold on, plot(sxxi(:,2))
%legend('Schist', 'Quartzite', 'Schist'),
ylabel('\sigma_{yy}^i (MPa)'), xlabel('Depth (m)')

subplot 514, plot(depth,(syyi-sxxi).*10.^-6) %plot(sxxi(:,1)), hold on,
plot(sxxi(:,2))
ylabel('\sigma_{yy}^i-\sigma_{xx}^i (MPa)'), xlabel('Depth (m)')
%legend('Schist', 'Quartzite', 'Schist')

subplot 515, plot(depth,(syyi-szzi).*10.^-6) %plot(sxxi(:,1)), hold on,
plot(sxxi(:,2))
ylabel('\sigma_{yy}^i-\sigma_{zz}^i (MPa)'), xlabel('Depth (m)')
%legend('Schist', 'Quartzite', 'Schist')

%Tensile Failure Check
TFC = zeros(M,N);
for j=1:3
for n=1:M
if szzi(n,j) >= (C(j)/2)                                    %(16 in Bourne, 2003)
    TFC(n,j) = 1;

end
end
end

%Shear Failure Check
SFC = zeros(M,N);
for j = 1:3
for n=1:M
if (szzi(n,j)-syyi(n,j))/2 >= (((C(j)*cos(theta)) -
((szzi(n,j)+syyi(n,j))*sin(theta))/2) %(20 in Bourne, 2003)
    SFC(n,j) = 2;
end
end
end

%Failure Criteria Matrix with Depth: 1 = tensile failure criteria met, 2 = shear
failure criteria met, 3 = both failure criteria met
FC = zeros(M,4);
FC(:, 1) = SFC(:,1) + TFC(:,1);
FC(:, 2) = SFC(:,2) + TFC(:,2);
FC(:, 3) = SFC(:,3) + TFC(:,3);
FC(:, 4) = depth(:,1);
```

Appendix B: Script for Thermally Influenced Exhumation

```
clear all
clc

%Define thicknesses of individual layers (17, 1.5, 10.5, 2.5, 0.5, 7.5, 11)
a = 17;
b = 1.5;
c = 10.5;
t = [a b c]; %thickness (meters)

%Define specific scenario parameters
    %SQS
    E = [30 80 30]*10^9;            %Young's moduli (Pa)
    nu = [0.2 0.23 0.2];            %Poisson's ratio
    C = [1.5 15 1.5]*10^6;          %cohesive strength of each layer (Pa)
(SomeUsefulNumbers & Zhang, 2011 Table 6)

%     %QSQ
%     E = [80 30 80]*10^9;            %Young's moduli (Pa)
%     nu = [0.23 0.2 0.23];           %Poisson's ratio
%     C = [15 1.5 15]*10^6;           %cohesive strength of each layer (Pa)
(SomeUsefulNumbers & Zhang, 2011 Table 6)

%Define non-specific scenario parameters
alpha = 10*10^-6;                   %thermal expansion coefficient (1/C)
rho = 2650;                         %density (kg/m^3)
g = 10;                             %grav acceleration (m/s^2)
N = length(E);                      %number of layers
M = 100;                            %number of iterations
lm = 0.4;                           %pore fluid factor (ratio of hydrostatic to
lithostatic pressure gradient)
mu = 0.75;                          %coeff of friction (SomeUsefulNumbers 0.5-0.8)
theta = 30*pi/180;                  %angle of internal friction

%Define individual layer coupling moduli (5 in Bourne, 2003)
m1i = E./(1- (nu).^2);
m2i = (nu.*E)./(1-(nu).^2);
m4i = nu./(1-nu);

%Define thickness averaged coupling moduli (6 in Bourne, 2003)
m1 = sum(m1i.*t)./sum(t);
m2 = sum(m2i.*t)./sum(t);
m4 = sum(m4i.*t)./sum(t);

%Define compound coupling moduli (8 in Bourne, 2003)
M1 = ((m1*m1i) - (m2*m2i))./(m1.^2-m2.^2);
M2 = ((m1*m2i) - (m2*m1i))./(m1.^2-m2.^2);
M4 = m4*((m1i+m2i)./(m1+m2))-m4i;



%Define regional stress path
h0 = 3000;              %initial depth
```

```
hf = 500;              %final depth
Tgrad = 25;            %geothermal gradient (degrees C per km)
T0 = Tgrad*h0./1000;   %starting temperature
Tf = Tgrad*hf./1000;   %final temperature

%Sibson Normal Fault Tensor
[syyb, sxxb, szzb] = Sibson_NormalFaultTensor(h0,lm,mu);        %calculate initial
stress state assuming normal faulting environment
sxxb = -sxxb*10^6;syyb = -syyb*10^6; szzb = -szzb*10^6;            %initial stress
state (Pa)

[syyf, sxxf, szzf] = Sibson_NormalFaultTensor(hf,lm,mu);        %calculate final
stress state assuming normal faulting environment
sxxf = -sxxf*10^6;syyf = -syyf*10^6; szzf = -szzf*10^6;            %final stress state
(Pa)

%Stress and Temperature Changes for Each Iteration
dsyy = linspace(0,(syyf-syyb), M+1);                            %vertical (greatest
compressive) stress path
dsxx = linspace(0,(sxxf-sxxb), M+1);                            %least compressive
stress path
dszz = linspace(0,(szzf-szzb), M+1);                            %intermediate
compressive stress path
dT = linspace(0,Tf-T0, M+1);                                    %temperature change

%Intialize layer stresses
sxxi = zeros(M,N);
syyi = zeros(M,N);
szzi = zeros(M,N);
syyi_isothermal = zeros(M,N);

for m = 1:M                                                     %loop that iterates
through each stress change increment
    for i = 1:N                                                 %loop that iterates
through each layer
        sxxi(m,i) =  sxxb + M1(i)*dsxx(m) + M2(i)*dszz(m) - M4(i)*dsyy(m) -
alpha*E(i)*dT(m)./(1-nu(i)); %(7 in Bourne, 2003)
        szzi(m,i) =  szzb + M1(i)*dszz(m) + M2(i)*dsxx(m) - M4(i)*dsyy(m) -
alpha*E(i)*dT(m)./(1-nu(i));
        syyi(m,i) =  syyb + dsyy(m) - alpha*E(i)*dT(m)./(1-nu(i));
        syyi_isothermal(m,i) =  syyb + dsyy(m);
    end
end

depth = syyi_isothermal./(rho*g*(1-lm));                        %depth (meters)

%Plot stress paths in each individual layer
figure,
subplot 511, plot(depth, sxxi.*10.^-6) %plot(sxxi(:,1)), hold on, plot(sxxi(:,2))
legend('Schist', 'Quartzite', 'Schist'),
ylabel('\sigma_{xx}^i (MPa)'), xlabel('Depth (m)')
```

```
subplot 512, plot(depth,szzi.*10.^-6) %plot(sxxi(:,1)), hold on, plot(sxxi(:,2))
%legend('Schist', 'Quartzite', 'Schist'),
ylabel('\sigma_{zz}^i (MPa)'), xlabel('Depth (m)')

subplot 513, plot(depth,syyi_isothermal.*10.^-6) %plot(sxxi(:,1)), hold on,
plot(sxxi(:,2))
%legend('Schist', 'Quartzite', 'Schist'),
ylabel('\sigma_{yy}^i (MPa)'), xlabel('Depth (m)')

subplot 514, plot(depth,(syyi-sxxi).*10.^-6) %plot(sxxi(:,1)), hold on,
plot(sxxi(:,2))
ylabel('\sigma_{yy}^i-\sigma_{xx}^i (MPa)'), xlabel('Depth (m)')
%legend('Schist', 'Quartzite', 'Schist')

subplot 515, plot(depth,(syyi-szzi).*10.^-6) %plot(sxxi(:,1)), hold on,
plot(sxxi(:,2))
ylabel('\sigma_{yy}^i-\sigma_{zz}^i (MPa)'), xlabel('Depth (m)')
%legend('Schist', 'Quartzite', 'Schist')

%Tensile Failure Check
TFC = zeros(M,N);
for j=1:3
for n=1:M
if szzi(n,j) >= (C(j)/2)                                    %(16 in Bourne, 2003)
    TFC(n,j) = 1;

end
end
end

%Shear Failure Check
SFC = zeros(M,N);
for j = 1:3
for n=1:M
if (szzi(n,j)-syyi(n,j))/2 >= (((C(j)*cos(theta)) -
((szzi(n,j)+syyi(n,j))*sin(theta))/2) %(20 in Bourne, 2003)
    SFC(n,j) = 2;
end
end
end

%Failure Criteria Matrix with Depth: 1 = tensile failure criteria met, 2 = shear
failure criteria met, 3 = both failure criteria met
FC = zeros(M,4);
FC(:, 1) = SFC(:,1) + TFC(:,1);
FC(:, 2) = SFC(:,2) + TFC(:,2);
FC(:, 3) = SFC(:,3) + TFC(:,3);
FC(:, 4) = depth(:,1);
```

Appendix C: Sibson Normal Fault Tensor

```
function [sig_v, sig_h, sig_H] = Sibson_NormalFaultTensor(d,lm, mu_s)

%determination of stress tensor based on R.H. Sibson, Frictional constraints on
thrust, wrench, and normal faults, Nature (1974)
%note: it is assumed that sig_H= mean normal stress = intermediate principal stress =
(sig_h+sig_v)/2

%theta = (angle between sigma 1 and fault)
%lm = (pore fluid factor - ratio of hydrostatic to lithostatic pressure gradient)
%mu_s = (static coefficient of friction)

theta_p = 0.5*atan2(1, mu_s);     %optimally oriented fault angle
rho = 2650;                       %mass density of rocks (kg/m3)
g = 10; %acceleration due to gravity (m/s)

R = (sin(2*theta_p)+mu_s*(cos(2*theta_p)+1))/(sin(2*theta_p)+mu_s*(cos(2*theta_p)-1));
sig_v = rho*g*d*(1-lm)*10^-6; %vertical princ stress (MPa) - *compression positive
sig_h = sig_v-(R/(1+R))*sig_v; %least compressive horizontal princ stress (MPa) -
*compression positive
sig_H = (sig_v+sig_h)/2; %greatest compressive horizontal princ stress (MPa) -
*compression positive
```